Journal of Materials Chemistry C

ROYAL SOCIETY OF CHEMISTRY

PAPER

View Article Online
View Journal

Cite this: DOI: 10.1039/d6tc00598e

Molecular precursor-directed growth of nanostructured SnS_2 for memristive and neuromorphic electronics

Suprabha S. Dixit, [a] Trishala R. Desai, [a] Omesh Kapur, [b] Bohao Ding, [b] Ruomeng Huang *[b] and Chitra Gurnani *[a]

Low-dimensional layered metal chalcogenides have recently garnered significant attention for advanced electronic and optoelectronic applications, particularly memristive and synaptic devices; however, achieving purity and scalable fabrication remains a key challenge. We demonstrate a facile and scalable *in situ* solvothermal approach enabling low-temperature deposition of SnS_2 thin films, employing the single-source precursor (SSP) $[Cl_2Sn(S_2P(O^iC_3H_7)_2)_2]$. The distorted octahedral complex $[Cl_2Sn(S_2P(O^iC_3H_7)_2)_2]$, derived from $SnCl_4$, serves as an efficient SSP for solvothermal growth of SnS_2 on ITO. The films exhibit phase-pure hexagonal crystallinity with well-defined composition and morphology, and an optical bandgap of 2.06 eV. Leveraging this synthesis route, Ag/SnS_2/ITO memristive device was fabricated, exhibiting electroforming-free bipolar resistive switching at ±0.6 V. The device demonstrated stable endurance over more than 10^2 cycles with an ON/OFF ratio of ~10. Additionally, the device further exhibits analogue conductance modulation and synaptic plasticity, enabling emulation of biological learning behaviour when implemented in a hardware-aware artificial neural network. The experimentally derived weight update dynamics achieved 92% classification accuracy on the MNIST dataset. Collectively, these findings establish SSP-derived SnS_2 thin films as a viable material platform for emerging memory and neuromorphic electronics.

Received 25th February 2026,
Accepted 18th May 2026

DOI: 10.1039/d6tc00598e

rsc.li/materials-c

1. Introduction

Tin disulphide (SnS_2), a layered post-transition metal chalcogenide, has emerged as a versatile material for energy, memory, and photonic applications due to its appropriate band gap (~2.2 eV)[1] high charge carrier mobility (~230 $cm^2\ V^{-1}\ s^{-1}$),[2] and robust chemical and thermal stability. As a group-IVA semiconducting metal chalcogenide composed of earth-abundant and environmentally benign elements, tin sulphide represents a low-cost materials platform. Structurally, SnS_2 adopts a CdI_2-type layered structure analogous to that of conventional transition metal dichalcogenides (TMDCs) (*e.g.*, MoS_2 and WS_2), resulting in weak interlayer van der Waals interactions and pronounced two-dimensional characteristics.[3,4] In addition, SnS_2 exhibits rich structural polymorphism, with more than seventy reported polytypes, including the 4H and 18R phases.[5] This hexagonal layered structure, bound by weak van der Waals interactions,[6] enables scalable fabrication of high-quality thin films suitable for device integration.[7]

Despite these advantages, conventional routes for the synthesis of SnS_2 thin films predominantly rely on dual-source precursor (DSP) systems, multistep processing, or hazardous sulphur reagents such as H_2S, which collectively limit process simplicity, safety, and scalability. In most reported studies, SnS_2 films are deposited from separate tin and sulphur sources (*e.g.*, $SnCl_4$ and H_2S), necessitating stringent control over precursor delivery to achieve stoichiometric composition while introducing significant handling and environmental concerns. To mitigate these challenges, a range of single-source precursors (SSPs) has been investigated, including thiolates and dithiolates such as $Sn(SCH_2CF_3)_4$, $Sn(SPh)_4$, $Sn(SCy)_4$,[8,9] and $Sn(SCH_2CH_2S)_2$,[10] dithiocarbamates and unsymmetrical dithiocarbamates such as $Sn(S_2CNEt_2)_4$,[11] and $\{RnSn[S_2CN(C_4H_9)CH_3]_{4-n}\}$, where R = Me, Bu, or Ph and n = 1, 2, or 3.[12] Nevertheless, a lot of these SSP systems still need external H_2S as an additional source of sulphur, post-deposition treatments, or binder-assisted processing, thereby increasing synthetic complexity and limiting scalability. In parallel, deposition of phase-pure SnS_2 thin films has largely relied on techniques that are costly, complex, and difficult to scale for large-area fabrication.[13] Common approaches

[a] Department of Chemistry, Ecole Centrale School of Engineering, Mahindra University, Hyderabad-500043, India.
E-mail: chitra.gurnani@mahindrauniversity.edu.in
[b] School of Electronics and Computer Science, University of Southampton, Southampton, UK. E-mail: r.huang@soton.ac.uk

include mechanical exfoliation,[3] chemical vapour deposition (CVD)[14,15] and physical epitaxy.[16] Although CVD and epitaxial growth can yield uniform films, their elevated processing temperatures often exceed the thermal budgets of technologically relevant substrates. Mechanical exfoliation, while capable of producing high-quality flakes, suffers from low yield and poor scalability.[17] Collectively, these limitations highlight the need for a one-pot, non-toxic, low-temperature, and scalable strategy for the controlled growth of pure-phase nanostructured SnS_2 thin films.

SSP strategies offer a compelling solution by integrating all requisite elements within a single molecular framework.[18] Such molecular-level stoichiometric preorganization enables precise compositional control while minimizing pre-reactions and sulphur deficiencies commonly encountered in DSP systems.[19] Moreover, rational modification of precursor structure provides a direct handle over decomposition pathways, phase selectivity, nucleation behavior, and film morphology, rendering SSP-based approaches particularly attractive for scalable thin-film fabrication. Herein, we focus on dithiophosphate (DTP) complexes as effective SSPs owing to their versatile coordination chemistry, preformed metal-sulphur bonds, and favorable thermal decomposition characteristics.[20] These attributes enable the formation of low-dimensional metal sulphides under relatively mild processing conditions while maintaining long shelf life and synthetic simplicity. Importantly, the tunability of the dithiophosphate framework further provides a molecular-level handle over precursor stability, volatility, and decomposition pathways, making this class of compounds particularly attractive for the scalable growth of phase-controlled tin sulphide thin films.[21] When combined with solution-based deposition strategies, such precursors offer a practical and scalable route for thin-film growth enables low-temperature and substrate-compatible deposition. This approach also provides control over phase purity, crystallinity, and film morphology, parameters that directly influence material properties. To date, no DTP-based molecular precursor has been reported for the direct low-temperature growth of phase-pure SnS_2 thin films.

The ability to achieve stoichiometric, binder-free, high-purity SnS_2 nanostructured thin films at low temperature through SSP-based routes provides a well-defined platform for electronic device applications. As artificial intelligence (AI) continues to advance, neuromorphic technologies that emulate biological neural networks are increasingly recognized as promising alternatives to conventional von Neumann architectures.[22,23] Within this landscape, SnS_2 has received comparatively less attention than other 2D materials[24,25] and/or transition metal dichalcogenides (TMDs),[26] such as MoS_2 and WS_2. Nevertheless, recent studies have begun to highlight its potential for neuromorphic applications.[27] In this context, liquid-phase-synthesised SnS_2 quantum dot memristors have demonstrated intriguing resistive switching characteristics.[28] SnS_2-reduced graphene oxide (rGO) composites have been explored as electrochemical artificial synapses,[29] while SnO_x/SnS_2 heterostructures have exhibited enhanced switching performance with relevance to neuromorphic technologies.[30] Very recently, spin-coated SnS_2 doped with Ca^{2+} ions has been reported for memristive behavior and synaptic emulation.[31] Collectively, these studies underscore the emerging potential of SnS_2 as an active material for next-generation neuromorphic architectures aimed at replicating the adaptive and learning functionalities of biological neural networks.

Herein, we report the synthesis and application of a new SSP, $[Cl_2Sn(S_2P(O^iC_3H_7)_2)_2]$, designed for low-temperature, one-step *in situ* solvothermal deposition of stoichiometric, crystalline SnS_2 thin films. This precursor enables direct growth of binder-free hexagonal SnS_2 on ITO/glass substrates under mild solvothermal conditions, and post-treatment. The resulting films exhibit well-defined nanostructured morphology and phase purity, validated through compositional and structural characterization. To demonstrate functional relevance, the solution-processed SnS_2 films were directly integrated into two-terminal resistive switching memory (RSM) devices. These devices demonstrated bipolar switching without forming or compliance, stable ON/OFF ratios and good endurance. Notably, the proposed pristine SnS_2-based memristors showed analog switching characteristics and synaptic behaviour, enabling emulation of biological plasticity and achieving 92% classification accuracy on the MNIST handwritten digit dataset in a hardware-aware artificial neural network (ANN) simulation.

2. Materials and methods

2.1 Reagents and materials

Tin tetrachloride ($SnCl_4$, 98%) and phosphorus pentasulphide (P_2S_5, 99%) were used as received from Alfa Aesar and Sigma-Aldrich, respectively. Toluene (C_7H_8, 99.5%), isopropanol (C_3H_8O, 99%), *n*-hexane (C_6H_{14}, 99%), and dichloromethane (DCM, CH_2Cl_2, 99.5%) were procured from S.D. Fine-Chem Limited, SRL, and FINAR, respectively. Every chemical was of analytical grade. Toluene and isopropanol were distilled before use. All experimental procedures were carried out in an inert atmosphere using vacuum and Schlenk-line techniques, with strict precautions to prevent exposure to moisture during handling. Global Nanotech provided glass substrates coated with indium tin oxide (ITO).

2.2 Synthesis of SSP and characterization

$[Et_3NH][(O^iC_3H_7)_2S_2P]$. The compound was prepared according to a previously described protocol for the propanol-based ligand.[32] P_2S_5 (2.5 g, 1.12 mM) was gradually added to distilled toluene (20 mL) under stirring, after which freshly distilled isopropanol (3.36 mL, 4.48 mM) was added. The mixture was heated at 80–90 °C until complete dissolution of P_2S_5, then cooled to ambient temperature. Triethylamine (Et_3N, 3.2 mL, 2.24 mM) was added dropwise under stirring, followed by the addition of *n*-hexane to induce precipitation. After filtration, the resulting white precipitate was dried under reduced pressure to remove residual solvents. Yield: (6.5 g, 88.3%); anal: M.W. of $C_{12}H_{30}O_2PS_2N$: 315.2; ^1H NMR ($CDCl_3$, 298 K, d ppm): 1.34 (t, [6H], $-CH_3$ of isopropanol), 1.42 (t, [9H], $-CH_3$ of Et_3N),

1.7 (m, [4H], $-CH_2CH_3$ of isopropanol), 3.3 (m, [4H], $-CH_2$ of isopropanol), 4.8 (m, [6H], CH_2 of Et_3N); $^{31}P\{^1H\}$ ($CDCl_3$, 298 K, d ppm): 107.48 (s); IR (KBr) (cm^{-1}): 1166(s), {ν[(P) O–C]}; 863(s), ν[P–O–(C)]; 660(s), ν(P═S) and 553(s), ν(P–S).

$Cl_2Sn[S_2P(O^iC_3H_7)]_2$. A suspension of {$[Et_3NH][(O^iC_3H_7)_2$-$S_2P]$}2 (2.025 g, 2.7 M) in toluene (20 mL) was prepared in an inert nitrogen atmosphere. Tin tetrachloride ($SnCl_4$, 0.377 mL, 0.9 M) was dropwise added to the suspension using a syringe, maintaining a 1 : 2 molar ratio in a nitrogen atmosphere. For 24 hours, at room temperature, the reaction mixture was agitated. Subsequently, it was filtered under anhydrous conditions to separate the triethylamine chloride precipitate. Concentration of the yellow filtrate under vacuum produced a yellow viscous oil. Upon incubation, the pale-yellow crystals formed spontaneously from the thick yellow oil. Yield: (1.81 g, 91%); anal: M.W. of $SnCl_2C_{12}H_{30}O_4P_2S_4$ = 426; ^1H NMR: ($CDCl_3$, 298 K, δ ppm): 5.3 (multiplet, 7H, $-CH_3$), 1.4 (doublet, 4H, –CH). $^{31}P\{^1H\}$ NMR: ($CDCl_3$, 298 K, δ ppm): 85.1 (singlet). $^{119}Sn\{^1H\}$ NMR: ($CDCl_3$, 298 K, δ ppm): 851.99 (t). IR (KBr) (cm^{-1}): 1177 (s), ν((P)–O–C), 960 (s), ν(P–O–(C)), 634 (s), ν(P═S), 536 (s), ν(P–S).

X-ray crystallography. $Cl_2Sn[S_2P(O^iC_3H_7)]_2$ diffraction results were obtained at 100(2) K using Mo Kα radiation (λ = 0.71073 Å) on an XtaLAB Synergy diffractometer equipped with a HyPix-3000 detector. ShelXL, as implemented in Olex232, was used to enhance the crystal structure after it was solved using the ShelXT structure-solving program.[33,34] Table S1 summarizes the crystallographic data and refinement details. The entire dataset, including structure factors, has been deposited at the Cambridge Crystallographic Data Centre (CCDC 2360486).

2.3 *In situ* solvothermal growth of nanostructured SnS_2 using $Cl_2Sn[S_2P(O^iC_3H_7)]_2$

Direct growth of SnS_2 thin films on ITO substrates was achieved *via* a one-step low-temperature solution-processed route employing $Cl_2Sn[S_2P(O^iC_3H_7)]_2$ as an SSP, as schematically shown in Fig. 1. A dispersion of $Cl_2Sn[S_2P(O^iC_3H_7)]_2$ (0.9 g) was prepared in freshly distilled, anhydrous isopropanol (20 mL) under a nitrogen atmosphere with continuous stirring for 30 min. The ITO-coated glass substrates were cleaned thoroughly using an ultrasonicator in a sequence of deionized water, ethanol, and acetone to ensure a pristine surface for film deposition. The cleaned ITO substrate was then positioned horizontally in the solution after it had been moved to a 20 mL Teflon-lined stainless-steel autoclave. The autoclave was kept at 200 °C for 24 hours, and then it was allowed to cool to ambient temperature. The resulting film was dried at 80 °C, leading to the formation of a nanostructured SnS_2 thin film on the ITO substrate.

2.4 SnS_2 thin fim characterization

A Rigaku SmartLab diffractometer using Cu Kα radiation (λ = 1.54 Å) was used to record X-ray diffraction (XRD) patterns throughout a 2θ range of 10–80°. A Bruker MultiRAM spectrometer was used to gather Raman spectra in the 120–1700 cm^{-1} range using an excitation source set at 514 nm. A Cary 5000 spectrophotometer (Varian, USA) was used to measure UV-visible absorbance spectra (wavelength range: 200–1000 nm). The elemental composition of SnS_2 thin films was determined by energy-dispersive X-ray spectroscopy (EDX) using an Oxford Instruments INCA Wave system, and the surface morphology was investigated using a Gemini/ZEISS ULTRA 55 scanning electron microscope (SEM). The adventitious C–C peak at 284.8 eV was used to calibrate binding energies for X-ray photoelectron spectroscopy (XPS) experiments, which were conducted using an AXIS SUPRA apparatus fitted with an Al Kα radiation source ($h\nu$ = 1486.6 eV). Infrared (IR) spectra were acquired using a Nicolet iS5 spectrometer (Thermo Scientific) over the wavenumber range of 4000–500 cm^{-1}. Nuclear magnetic resonance (^1H NMR, $^{31}P\{^1H\}$ NMR, and $^{119}Sn\{^1H\}$ NMR) measurements were carried out on a Bruker Avance Neo 500 MHz spectrometer in $CDCl_3$ at ambient temperature.

2.5 SnS_2 memristor fabrication and electrical characterization

Memristive devices were constructed using solvothermally synthesized SnS_2 thin films as the active switching layer,

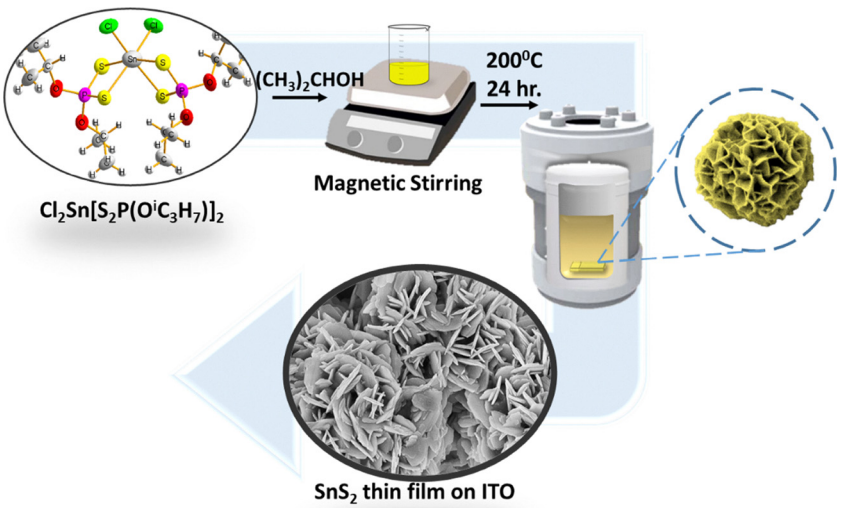

Fig. 1 Schematic illustrations of *in situ* growth of SnS_2 nanostructured thin film using SSP on ITO.

deposited ITO-coated glass substrates (2×1 cm^2), which served as the bottom electrode. The thickness of the SnS_2 layer was approximately 7.38 μm. A silver (Ag) top electrode, ~100 nm in thickness with an effective device area of ~1 mm^2, was formed on the SnS_2/ITO structure using conductive silver paste. Electrical characterization was carried out at room temperature under ambient conditions using a Keysight B1500 semiconductor parameter analyzer, while pulsed switching measurements were conducted with a B1530 waveform generator/fast measurement unit (WGFMU). During measurements, bias voltage was applied to the top Ag electrode, with the ITO bottom electrode maintained at ground potential. Temperature-dependent DC-IV characteristics were evaluated using a Linkam FTIR600 heating stage equipped with a T96 LinkPad temperature controller.

2.6 Simulation for MNIST pattern recognition

To evaluate the neuromorphic capability of the SnS_2 memristor, conductance modulation was experimentally obtained using potentiation and depression pulse trains. The measured currents were converted to conductance values and normalized to the range [0,1], serving as discrete synaptic weight levels in network simulations. A fully connected multilayer perceptron ($784 \times 512 \times 10$) was implemented, corresponding to flattened 28×28 MNIST images. ReLU activation functions were used, and bias terms were excluded to maintain compatibility with memristive hardware architectures. The MNIST dataset was split into 50 000 training, 10 000 validation, and 10 000 test samples. Training employed a batch size of 10 000 with an effective learning rate of 3.91×10^{-3}, obtained by linearly scaling a base rate of 1.0×10^{-3} (base batch size: 256). To reflect discrete device updates, weights were quantized to the nearest experimentally measured conductance level every two epochs. Simulations were performed on a Windows 11 system with an AMD Ryzen 7950X CPU and an NVIDIA RTX 4090 GPU.

3. Results and discussion

3.1 Single source precursor characterisation

$[Et_3NH][(O^iC_3H_7)_2S_2P]$. The characterization of the diisopropyl dithiophosphate ligand $[Et_3NH][(O^iC_3H_7)_2S_2P]$ was confirmed through IR, ^{1}H NMR, and $^{31}P\{^1H\}$ NMR spectroscopy. The IR spectrum displays all characteristic bands in their expected regions (Fig. S1). The ^{1}H NMR spectrum (Fig. S2) shows all the relevant peaks corresponding to the protons of the $[Et_3NH][(O^iC_3H_7)_2S_2P]$ ligand. Furthermore, the $^{31}P\{^1H\}$ NMR spectrum (Fig. S3) presents a sharp singlet at 110.66 ppm, indicating the symmetrical nature of the molecule in solution and confirming the equivalent chemical environment of the phosphorus nuclei.

$Cl_2Sn[S_2P(O^iC_3H_7)]_2$. The purity and composition of the dichlorotin(IV) bis(*O*,*O*-diisopropyl dithiophosphate) $[Cl_2Sn(S_2P(O^iC_3H_7)_2)_2]$ complex were established using IR, ^{1}H, $^{31}P\{^1H\}$, and $^{119}Sn\{^1H\}$ NMR spectroscopy, together with SCXRD analysis. The IR spectrum of the complex (Fig. S4) was interpreted by comparison with that of the free ligand, $[Et_3NH][(O^iC_3H_7)_2S_2P]$, providing insight into ligand coordination and bonding interactions. Strong absorption bands observed in the 1180–1144 cm^{-1} and 893–784 cm^{-1} regions were assigned to the asymmetric and symmetric stretching vibrations of the P–O–C moiety, respectively. A medium-intensity band at 680.7 cm^{-1} was attributed to P═S symmetric or P–S asymmetric stretching vibrations. This band exhibits a downward shift of approximately 10–40 cm^{-1} relative to the free ligand, which is attributed to coordination of sulphur from the P═S group to the Sn(IV) centre. Additional bands near 510 cm^{-1} were assigned to P–S stretching vibrations, further supporting metal–sulphur coordination.

The ^{1}H NMR spectrum (Fig. S5) of the $Cl_2Sn(S_2P(O^iC_3H_7)_2)_2$ complex was recorded in $CDCl_3$ at room temperature. A sharp doublet for the methyl protons was observed at 1.468–1.474 ppm, very close to the reported values for $[Et_3NH][(O^iC_3H_7)_2S_2P]$, with a negligible shift of ~0.01 ppm. The isopropyl protons, perceived as a multiplet in the 5.314–5.390 ppm region, show a coordination-induced shift of ~0.4 ppm relative to the corresponding salts. These small downfield shifts confirm ligand coordination to the metal centre, while the overall negligible changes are attributed to the large separation between tin and the hydrogen nuclei.

The $^{31}P\{^1H\}$ NMR spectrum (Fig. S6) of the $Cl_2Sn(S_2P(O^iC_3H_7)_2)_2$ complex, recorded in $CDCl_3$, displays a single sharp resonance at 85.1 ppm, confirming coordination of the dithiophosphate groups to the metal centre. The presence of a singlet indicates that all phosphorus nuclei are chemically equivalent, corresponding to a single phosphorus environment in solution. Relative to the free ligand, this resonance exhibits a downfield shift of approximately 12 ppm, which is attributed to dative P═S → M interaction, reflecting the anisobidentate coordination mode of the dithiophosphate moiety[35] of dithiophosphate moieties. This assignment is further supported by the determination of Glidewell, which correlates $^{31}P\{^1H\}$ chemical shifts in the 82–101 ppm range with bidentate ligand coordination.[36]

Fig. S7 represents the ^{119}Sn $\{^1H\}$ NMR spectrum of the $Cl_2Sn[S_2P(O^iC_3H_7)]_2$ complex, which exhibits a triplet in the region 852.32 to 851.61 ppm. The $J(^{119}Sn–^{31}P)$ values of the chloro derivatives lie in the range 60–64.38 Hz, close to those observed in dihalotin(IV) dialkyldithiophosphates $^{119}Sn\{H\}$ NMR, supporting bidentate chelation.[37]

The compound *cis*-$Cl_2Sn[S_2P(O^iC_3H_7)]_2$ crystallized in the orthorhombic system with space group $C222_1$. Fig. 2 clearly illustrates that tin (Sn) lies at the centre of a distorted octahedron with symmetrically chelating bidentate dithiophosphate moieties and two chlorine atoms occupying *cis* positions. The list of bond distances and angles is given in Tables S2 and S3. The mutually *trans* Sn–S distances are shorter [Sn(1)–S(1) = 2.5138 Å and Sn(1)–S(3) = 2.52(2) Å] than the Sn–S distances *trans* to halide [Sn(1)–S(2) = 2.59(1) Å and Sn(1)–S(4) = 2.59(16) Å]. These bond distances are comparable to those observed in $I_2Sn[S_2P(C_2H_5)_2]_2$ (2.535 Å and 2.601 Å)[38] thus emphasizing anisobidentate coordination of ligand moieties in the compound. The average P–S bond lengths are [S(2)–P(1) and S(4)–P(1) = 2.004 Å; S(1)–P(1) and S(3)–P(2) = 2.002 Å]. The two dithiophosphate moieties depict both equatorial and axial coordination, where S(4)–Sn(1)–Cl(1) forms the axial plane and

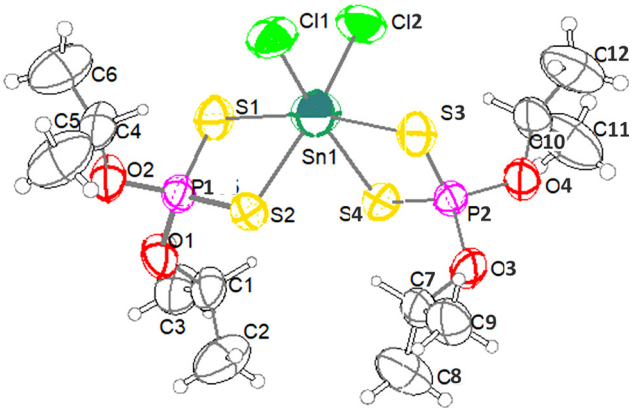

Fig. 2 ORTEP Plot of the $Cl_2Sn[S_2P(O^iC_3H_7)]_2$.

S(2)–S(1)–Sn(1)–S(3)–Cl(2) forms the equatorial plane with a dihedral angle of 90.39°. The Cl(1)–Sn(1)–Cl(2) bond angle is 93.23°, reflecting *cis* orientation, and is quite comparable to that observed in $I_2Sn[S_2PEt]_2$ [I(1)–Sn–I(2) = 92.33°].[39] The S–Sn–S bite angles 78.65(6)° and 78.33(6)° are similar to the values in $Cl_2Sn[S_2COEt]_2$[40] [70.63(5)° and 71.15(5)°] and $Br_2Sn[S_2COEt]_2$ [70°, 76.8°].[40] The interligand angles involving tin and sulphur [88.14(7)° to 168.06(9)°], and Cl(2)–Sn–S(2) = 90.39(7)°, depict distortion from the octahedral arrangement of Sn around ligand moieties. The S–P–S angles [109.69°–109.12°] and O–P–O angles [98.40°–98.80°] suggest that the phosphorus atom of the dithiophosphate ligands is located at the centre of a distorted tetrahedron.

To contextualize the advantages of the present SSP, a comparative analysis with previously reported tin-based SSPs for SnS_2 deposition is presented in Table S4. Most reported systems require external sulphur sources, reflecting incomplete precursor decomposition and poor stoichiometric control. Sulphur deficiency also remains a common limitation, adversely affecting material quality. In contrast, the present DTP-based SSP enables low-temperature (200 °C), one-step solvothermal synthesis without any external sulphur source, while maintaining stoichiometric sulphur incorporation. Importantly, unlike most previously reported systems where device integration is either unexplored or limited to energy applications, the synthesized SnS_2 in this work is the first demonstration in a memristive and neuromorphic device, underscoring its functional applicability in advanced electronics.

3.2 Structural and morphological studies of SnS_2 thin film

SnS_2 nanostructured thin films were fabricated *via* a one-step, low-temperature *in situ* solvothermal process employing $Cl_2Sn[S_2P(O^iC_3H_7)]_2$ as a SSP, as schematically depicted in Fig. 1. This solvothermal strategy enables a straightforward route to form nanostructured thin layers through precursor decomposition in isopropanol. The as-prepared SnS_2 films were subsequently examined by XRD, Raman spectroscopy, SEM, and XPS to investigate their structural, morphological, and chemical characteristics.

The crystal structure and phase purity of the synthesized SnS_2 nanostructures were elucidated using X-ray diffraction (XRD). As illustrated in Fig. 3a, the acquired diffraction pattern exhibits excellent agreement with the standard reference data for the SnS_2 (ICDD card no. 084-9283). The prominent diffraction peaks located at values of 15.0°, 28.1°, 32.2°, 41.8°, and 50.0° are indexed to the (001), (100), (101), (102), and (110) crystallographic planes, respectively. This confirms the successful formation of a high-purity, solution-processed SnS_2 thin film crystallizing in the hexagonal system (space group $P\bar{3}m1$).[41–43] To further quantify the structural parameters, Rietveld refinement was performed on the XRD data (Fig. S8). The refinement converged successfully, yielding high-quality fit metrics (R_{wp} = 4.43%, R_p = 3.28%, GoF(χ^2) =1.6112, S = 1.2693, and V = 500.918 Å) and an extracted unit cell volume of V = 500.918 Å. The refined lattice parameters (a = b = 3.649 Å, and c = 5.91 Å) closely match the standard literature values (a = b = 3.646 Å, and c = 5.893 Å). Finally, the average crystallite size (D_c) of the SnS_2 nanostructures was calculated to be 24.63 nm using the Debye–Scherrer relation (1).

$$D_c = \frac{0.9\lambda}{\beta \cos\theta} \quad (1)$$

The X-ray wavelength is represented by λ, the full width half maximum (FWHM) by β, and Bragg's diffraction angle by θ.

Furthermore, a detailed structural analysis has been incorporated, including microstructural parameters derived from peak broadening. The lattice microstrain was calculated using the relation $\varepsilon = \beta/(4\tan\theta)$, yielding an average value of $\sim 6.4 \times 10^{-3}$, (Table S5), indicating moderate lattice distortion arising from defects within the thin film. The texture coefficient (TC) was also calculated using the relation (2),

$$TC(hkl) = \frac{I(hkl)/I_0(hkl)}{\frac{1}{n}\sum I(hkl)\Big/ I_0(hkl)} \quad (1)$$

ehere, $I(hkl)$ and $I_0(hkl)$ represent the measured and standard intensities, respectively, and n is the number of diffraction peaks considered. The calculated TC values of 1.7 and 1.07 for the (100) and (110) planes, respectively, indicate that the (100) plane exhibits a stronger preferred orientation due to its higher TC value, reflecting anisotropic crystallite alignment in the SnS_2 thin film.

The crystalline nature of the as-deposited SnS_2 thin film was further confirmed by Raman spectroscopy (Fig. 3b). The most intense peak at 315 cm^{-1} corresponds to the A_{1g} mode, signifying the vertical out-of-plane vibration between S–S, and the E_g mode (205 cm^{-1}) corresponds to the non-degenerate in-plane vibrations[44,45] consistent with the 2H-SnS_2 phase.[45]

The SEM image (Fig. 3c) shows the formation of SnS_2 nanoflowers like morphology composed of radially assembled ultrathin 2D nanosheets, highlighted in the high-magnification inset. The nanoflowers exhibited diameters ranging from approximately 800 nm to 1.2 μm, with individual nanosheets of 20–30 nm thickness. These SnS_2 nanoflowers exhibit abundant edge sites, resulting from the random stacking and arrangement of the SnS_2 nanosheets. Fig. 3d shows the EDX spectra of the SnS_2 thin film, and the resulting peaks suggest

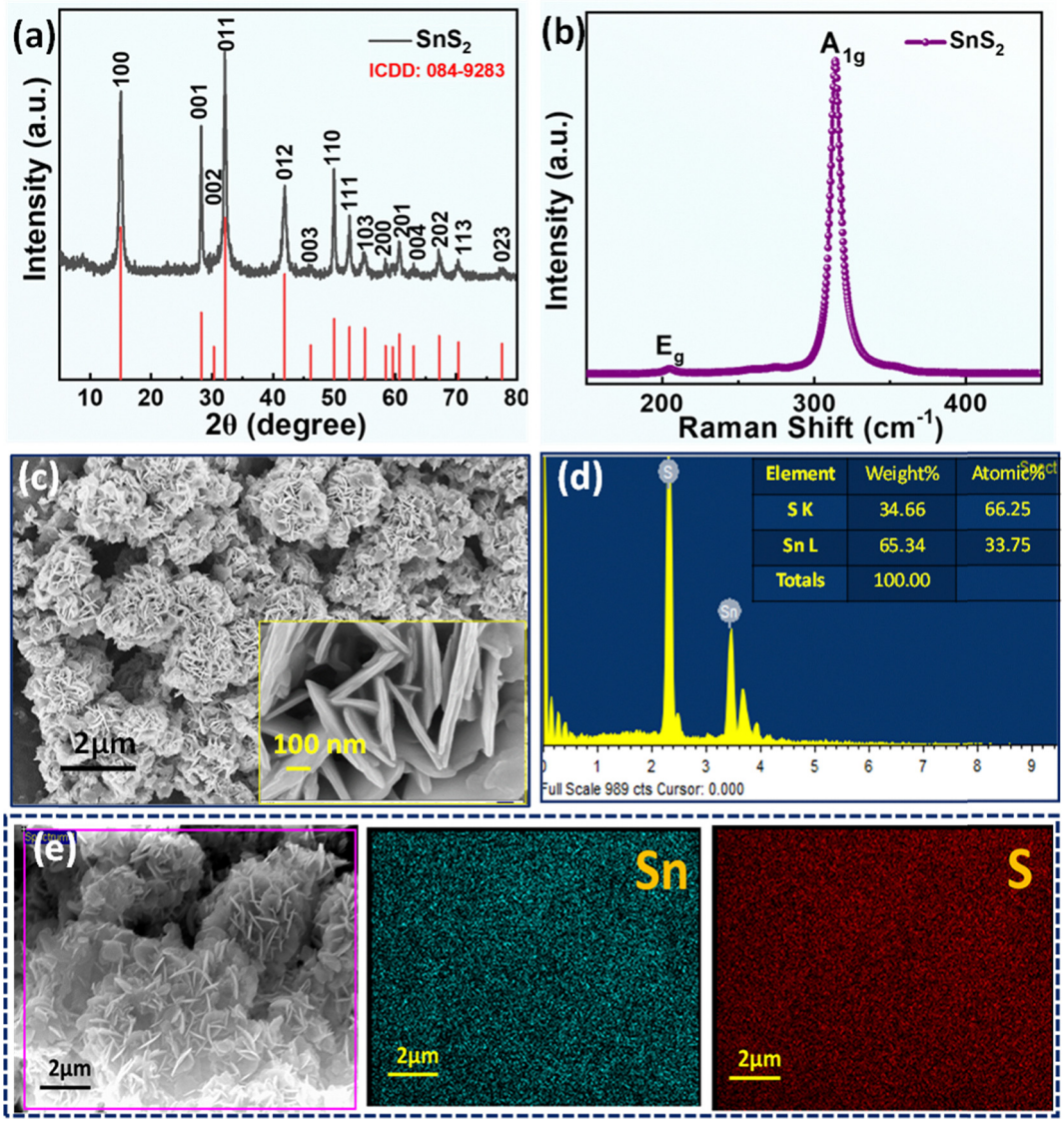

Fig. 3 (a) XRD, (b) Raman, (c) FESEM, (d) EDX spectrum with the percentage of elements, and (e) EDX elemental mapping of as-deposited SnS_2 nanostructured thin film on ITO.

the presence of tin and sulphur with an atomic percentage of 1 : 2 ratio, consistent with the expected composition of SnS_2. The EDX elemental mapping in Fig. 3e further confirms the uniform spatial distribution of Sn and S within the SnS_2 nanostructured thin film. Cross-sectional SEM analysis revealed that the SnS_2 film possesses a thickness of approximately 7.38 μm (Fig. S9).

The stoichiometric composition and oxidation states of Sn and S in the SnS_2 nanostructured thin film were investigated using XPS measurements (Fig. 4a). The high-resolution deconvoluted XPS spectra of the Sn 3d and S 2p core levels (Fig. 4b and c) exhibit well-resolved peaks without any satellite features, confirming the chemical purity of the as-deposited SnS_2 film. Sn 3d reveals two prominent peaks at 492.1 eV (Sn $3d_{5/2}$), and 486.7 eV (Sn $3d_{3/2}$), which are in good accordance with the Sn^{4+} state of SnS_2. No peak was detected at a binding energy of 485.8eV, indicating that Sn^{2+} is absent.[43] Further S $2p_{1/2}$ and S $2p_{3/2}$ peaks appeared at 162.8 and 161.7 eV, respectively attributes to the S^{2-} oxidation state. The doublet separation of SnS_2 was represented with the binding energy gap of 1.1 eV between the two peaks.[46] The absence of the O 1s peak at 531 eV confirms the formation of pure SnS_2 thin film.[47] UV-vis spectrum (Fig. 4d) was employed to analyze the optical absorption properties of SnS_2 thin film. The absorption spectra of the as-synthesized SnS_2 layer absorb maximum light in the higher wavelength region (350–500 nm). The optical bandgap energy (E_g) of SnS_2 thin film was determined using the Tauc eqn (3):

$$\alpha h\nu = A(h\nu - E_g)^{n/2} \quad (3)$$

The absorption coefficient is denoted by α, the optical band gap energy by E_g, the light frequency by ν, the Planck's constant by h, and a constant by A. The value of n is determined by the nature of the electronic transition; for direct transitions, it is 1, while for indirect transitions, it is 4. From the Tauc plot of

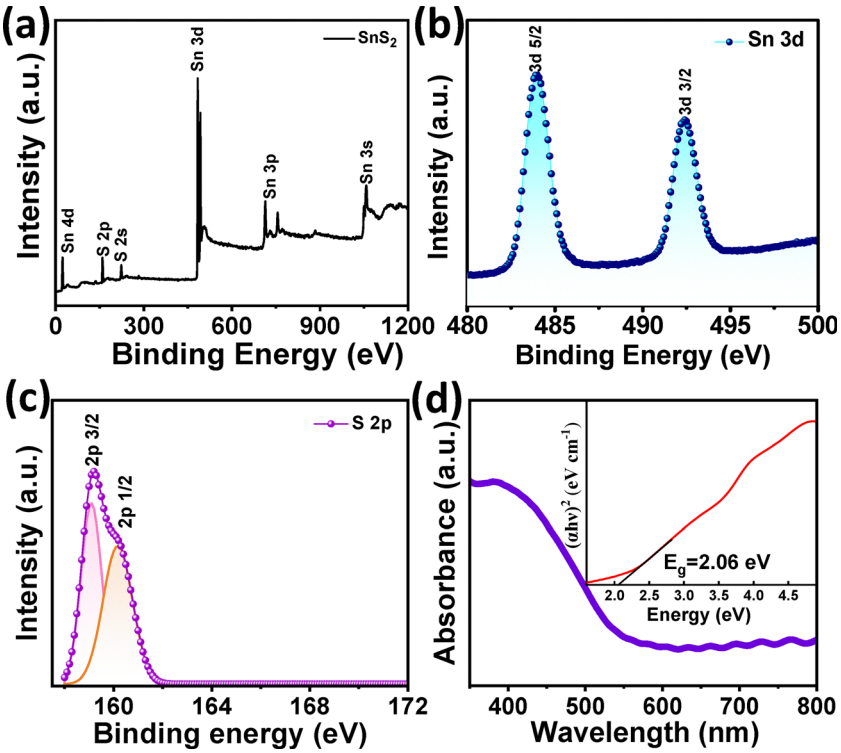

Fig. 4 (a) High-resolution XPS spectra and the XPS survey spectrum of (b) Sn 3d and (c) S 2p spectra, (d) Absorption spectra with bandgap analysis of SnS_2 thin film on ITO.

$(\alpha h\nu)^2$ *versus* $h\nu$, the bandgap energy of SnS_2 thin film was obtained to be 2.06 eV. It was found that the observed band gap energy matched within the range of those reported in the literature.[48,49]

3.3 SnS_2 memristor characterisation

The memristive switching behaviour of the SnS_2 film was evaluated by incorporating the as-deposited layer into a two-terminal Ag/SnS_2/ITO device for DC *I–V* measurements. The SnS_2 active layer is positioned between an ITO bottom electrode and a silver (Ag) top electrode in the schematic cross-section of the device (Fig. 5a). In its pristine state, a positive voltage sweep from 0 to 0.6 V causes the device to transition from its high-resistance state (HRS) to a low-resistance state (LRS) (Fig. 5b). The HRS is restored by a later negative sweep. Both the SET and RESET transitions occur without requiring a compliance current. The reproducibility of the SET voltage and the absence of any initial high-voltage transition confirm that the device operates in an electroforming-free manner. Such forming-free, compliance-free switching is highly desirable for high-density integration, particularly in crossbar architectures. The device maintains stable switching over 100 DC cycles, with an ON/OFF ratio of approximately one order of magnitude (Fig. 5c). Both HRS and LRS remain reasonably stable with only minor drift. Retention characteristics of the SnS_2 memristor were evaluated by monitoring the resistance states of both HRS and LRS at room temperature under a constant read voltage of 0.1 V. As shown in Fig. 5d, the device maintains clearly distinguishable resistance states for over 1200 s without noticeable degradation or state overlap, indicating stable non-volatile switching behaviour. Importantly, both states exhibit negligible resistance drift during the measurement period, suggesting excellent stability. Notably, when the SET/RESET voltages are reduced to ±0.4 V, the device accesses intermediate resistance levels (Fig. 5e), demonstrating voltage-dependent conductance modulation. This multi-level behaviour is an essential requirement for neuromorphic computing and analogue memory applications. The conduction mechanism was further analysed by plotting the SET I–V response on a logarithmic scale (Fig. 5f). In the HRS, the device follows the space-charge-limited current (SCLC) model: an initial Ohmic region (0–0.1 V) attributed to thermally generated carriers, followed by a trap-controlled SCLC regime ($I \propto V^2$) between 0.1 and 0.3 V, before transitioning sharply to the LRS. Once switched, the device returns to Ohmic conduction in the LRS.

Temperature-dependent *I–V* measurements of the LRS between 20 to 80 °C (Fig. 6a) reveal metallic conduction, as the inset illustrates, resistance drops linearly with temperature. From the slope, the temperature coefficient of resistance (TCR) is extracted as 1.4×10^{-3} K^{-1}, consistent with values typically reported for nanoscale Ag filaments,[50] confirming that metallic Ag pathways dominate charge transport in the LRS. To further support the proposed switching mechanism, temperature-dependent measurements were also performed for the HRS at a fixed read voltage of 0.1 V (Fig. 6b). In contrast to the LRS, the current increases with increasing temperature, corresponding to a decrease in resistance with temperature, which is characteristic

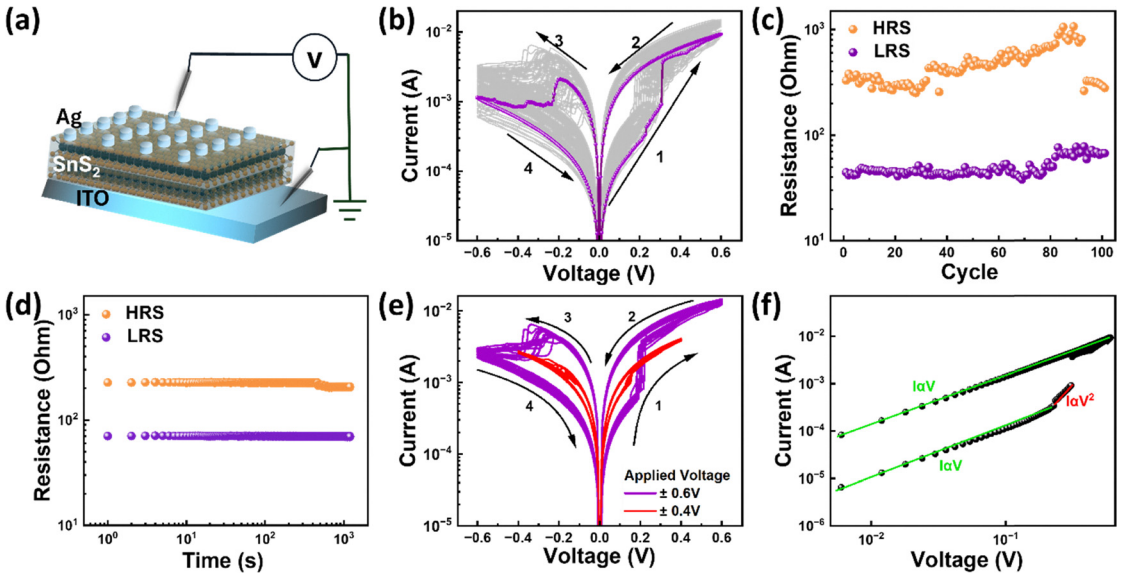

Fig. 5 (a) Schematic illustration of the Ag/SnS_2/ITO memristor structure. (b) Consecutive DC *I*–*V* switchaing characteristics measured of 100 cycles under voltage sweeps of ±0.6 V, (c) Endurance performance over 100 DC switching cycles, demonstrating stable bipolar resistive switching with an ON/OFF ratio of ~10. (d) Retention characteristics of the SnS_2 memristor for both the HRS and LRS measured at room temperature under a read voltage of 0.1 V. (e) DC *I*–*V* characteristics under different voltage ranges, showing electroforming-free bipolar switching at ±0.6 V and multilevel resistive switching at ±0.4 V. (f) log–log *I*–*V* plot during the SET process, indicating trap-controlled SCLC in the HRS and Ohmic conduction in the LRS.

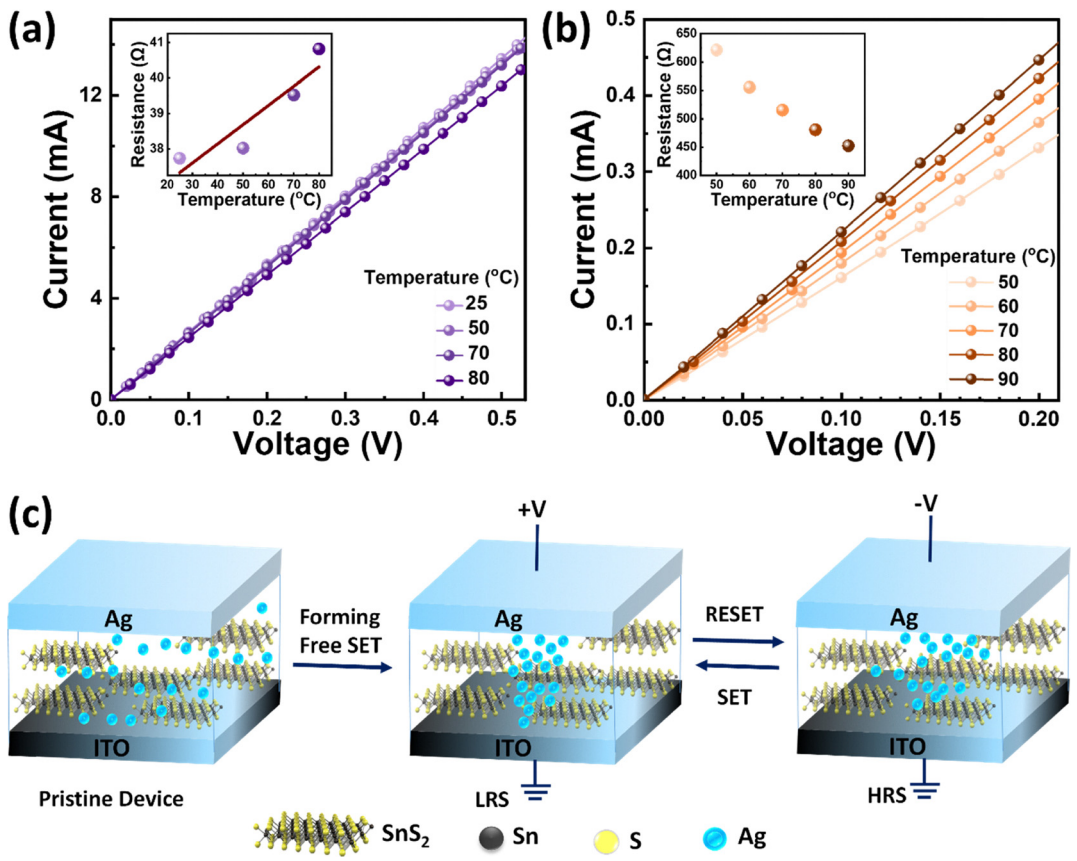

Fig. 6 (a) Temperature-dependent *I*–*V* curves in LRS measured from 20 to 80 °C. The inset shows the linear decrease in resistance with increasing temperature, yielding a TCR of 1.4×10^{-3} K^{-1}, consistent with metallic Ag conduction. (b) Temperature-dependent *I*–*V* characteristics of the SnS_2 memristor in the HRS measured from 50 to 90 °C. The inset shows the corresponding resistance as a function of temperature at a read voltage of 0.1 V, where the resistance decreases with increasing temperature. (c) Schematic illustration of the proposed resistive switching mechanism based on the formation and rupture of conductive Ag filaments within the SnS_2 layer.

of thermally activated semiconducting transport. This behaviour is consistent with the trap-controlled SCLC mechanism identified from Fig. 5f. In the HRS, charge transport is dominated by thermally generated carriers and trap-assisted conduction through the SnS_2 layer, where increasing temperature facilitates carrier de-trapping and enhances conduction. The distinct temperature-dependent behaviours of the LRS and HRS further support the filamentary switching mechanism. Based on these results, we propose a filamentary switching mechanism for the SnS_2 memristor, involving the rupture of Ag conductive filaments and electrochemical formation inside the SnS_2 matrix, as illustrated in Fig. 6c. The device changes from the HRS to the LRS when Ag ions migrate and are reduced to create metallic filaments that bridge the electrodes under positive bias. Conversely, under reverse bias, the filament dissolves or ruptures, restoring the device to the HRS. The memristive performance is closely related to the intrinsic material properties of the solvothermally deposited SnS_2 film. The measured optical band gap of $\sim$2.06 eV provides a suitable balance between charge transport and carrier confinement, contributing to the low switching voltage and reduced leakage current.[51] In addition, the nanoflower-like morphology composed of interconnected nanosheets increases the effective surface area and introduces abundant grain boundaries and defect sites, which facilitate localized electric field enhancement and defect-assisted Ag ion migration during conductive filament formation.[26] Combined with the good crystallinity of the hexagonal SnS_2 phase and the trap-controlled SCLC behaviour observed in the HRS, these structural features indicate that intrinsic defects and interfacial trap states play an important role in charge trapping and transport, thereby influencing the switching voltage, resistance window, and analogue conductance modulation behaviour. Although device-to-device variation in switching current and resistance window is observed (Fig. S10), the consistent bipolar switching polarity and similar operating voltage indicate good reproducibility of the underlying filamentary switching mechanism. The observed variation is mainly attributed to the morphological inhomogeneity and local thickness variation of the solution-processed SnS_2 films. Further optimisation of film uniformity and device reproducibility is part of our ongoing work.

The observed RS behaviour of the SnS_2 thin films can be attributed to their intrinsic material properties and morphology. The optical band gap ($\sim$2.06 eV) facilitates efficient charge transport while maintaining a suitable energy barrier for carrier injection, contributing to the low switching voltage and reduced leakage current.[51] The nanoflower-like morphology, composed of interconnected SnS_2 nanosheets, provides a high density of active sites along with localized electric field enhancement,

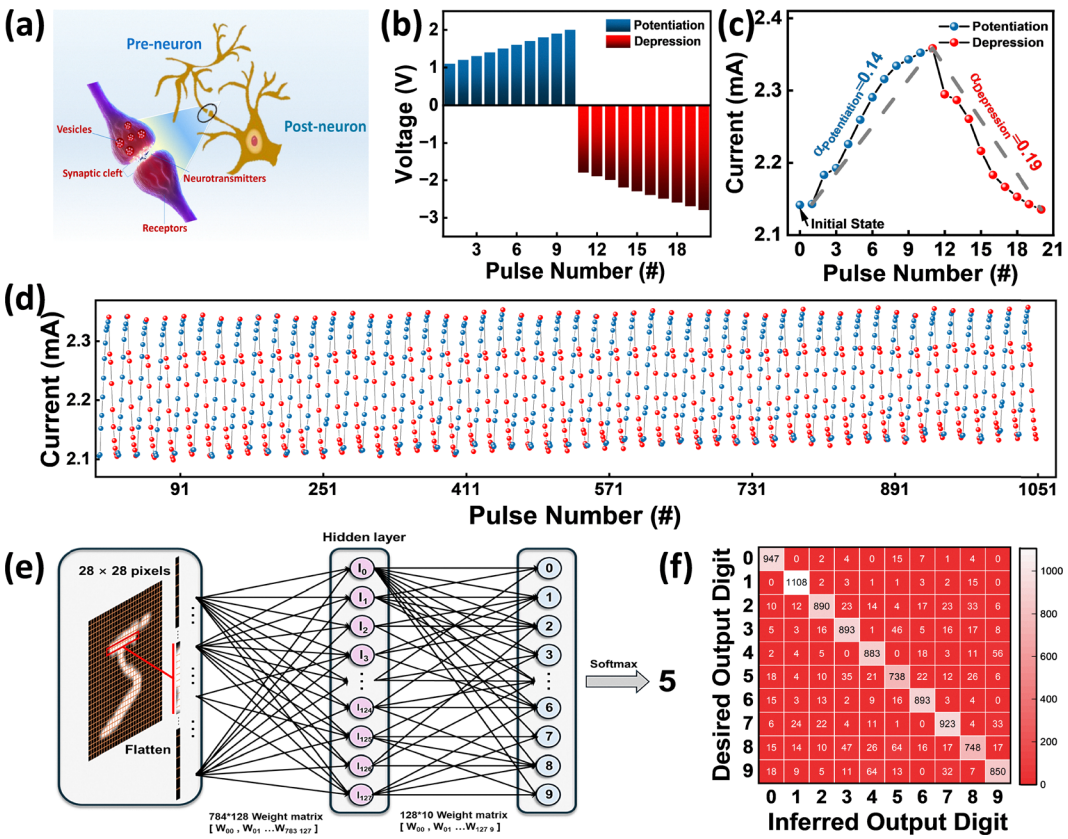

Fig. 7 Synaptic weight modulation and neural network simulation based on SnS_2 memristor. (a) Biological synapse schematic depiction. (b) Staircase pulses applied to the memristor. (c) Characteristics of long-term potentiation (LTP) and depression (LTD) under staircase pulse stimulation. Linearity analysis of LTP/LTD showing $\alpha_{potentiation}$ = 0.14 and $\alpha_{depression}$ = 0.19. (d) Stability over 50 repeated LTP/LTD cycles. (e) Schematic of ANN architecture for MNIST classification using extracted synaptic behaviour. (f) Confusion matrix showing 92% test accuracy.

which promotes defect-assisted conductive filament formation and ensures stable switching characteristics.[26] Furthermore, the layered van der Waals structure of SnS_2 offers favourable pathways for ion migration. The relatively large interlayer spacing, compared to the ionic radius of the active electrode species, minimizes lattice distortion during ion migration and filament formation, thereby lowering the SET voltage.[52]

In biological synapses, signal transmission and processing are governed by the modulation of Ca^{2+} and K^+ ion concentrations across the synaptic cleft (Fig. 7a). Emulating such synaptic behaviour is crucial for developing core building blocks in neuromorphic systems. To demonstrate this capability, we evaluated the synaptic plasticity of our SnS_2-based memristor by applying a series of pulsed stimuli that mimic synaptic weight modulation (Fig. 7b). Specifically, the device was subjected to ten positive voltage pulses (each 50 μs wide) with a staircase amplitude from 1.1 V to 2 V, followed by ten negative pulses ranging from −1.8 V to −2.8 V. Under positive stimulation, the device exhibited a gradual increase in current, indicative of LTP, while the application of negative pulses led to a progressive decrease in current, corresponding to LTD. The linearity of these conductance updates was quantified using the α-metric developed by Wang *et al.*,[53] yielding $\alpha_{potentiation} = 0.14$ and $\alpha_{depression} = 0.19$ (Fig. 7c), which reflects excellent linear weight modulation, a key requirement for analogue neuromorphic computing. This behaviour remained consistent over 50 consecutive LTP/LTD cycles, as shown in Fig. 7d, demonstrating the robustness and potential of the device for reliable synaptic emulation.

A fully connected artificial neural network (ANN) simulation was performed to evaluate the effects of the empirically observed synaptic weight modulation on learning using the extracted potentiation and depression characteristics. 784 input neurons, which correspond to the flattened 28 × 28-pixel MNIST images, 512 hidden neurons, and 10 output neurons, which represent the digit classes (0–9), comprise the ANN. (Fig. 7e) Fig. S11 shows the validation accuracy during training. The final classification performance was assessed on the test set, yielding an accuracy of 92%, as summarized in the confusion matrix in Fig. 7f. These results demonstrate the effective translation of the device-level synaptic characteristics into system-level learning performance, highlighting the strong potential of our SnS_2 memristor for neuromorphic computing applications.

To benchmark the performance of our memristor, we compare it with representative SnS_2-based memory devices reported in the literature (Table S6). Although previously reported systems exhibit promising switching characteristics, they generally rely on multi-step fabrication processes (*e.g.*, hydrothermal synthesis followed by spin coating),[31] high-temperature treatments (≥300 °C),[54] or seed layers to achieve uniform film growth.[26] Moreover, many of these devices require an electroforming step, which can increase power consumption and affect long-term reliability. In contrast, our approach employs a molecularly designed SSP to enable a one-step, low-temperature (200 °C), and *in situ* solvothermal deposition process, yielding stoichiometric SnS_2 films. The simplified synthesis, compatibility with flexible substrates, forming-free switching behavior, and demonstration of neuromorphic functionalities collectively underscore the specific advantages and technological significance of this system.

4. Conclusion

In summary, we demonstrate the *in situ* solvothermal, low-temperature growth of crystalline SnS_2 thin films using the dithiophosphate-based SSP $[Cl_2Sn(S_2P(O^iC_3H_7)_2)_2]$. The distorted octahedral complex $[Cl_2Sn(S_2P(O^iC_3H_7)_2)_2]$, synthesized from $SnCl_4$, was comprehensively characterized by IR, multinuclear NMR (^1H, $^{31}P\{^1H\}$, $^{119}Sn\{^1H\}$), and SCXRD analyses, which confirmed its molecular structure. This well-defined precursor enables direct deposition of uniform, phase-pure hexagonal SnS_2 nanostructured films on ITO/glass substrates without external sulphur sources or post-treatment. The resulting films exhibit high crystallinity and chemical purity and function effectively as the active layer in Ag/SnS_2/ITO memristive devices. The devices exhibit electroforming-free bipolar resistive switching with low operating voltages (0.6 V) and compliance-free operation, along with stable endurance (>100 cycles) and an ON/OFF ratio of ∼10. Temperature-dependent electrical analyses confirm a filamentary switching mechanism governed by metallic Ag conduction. In addition, the pristine SnS_2 films display analog resistive modulation and synaptic behavior, achieving 92% classification accuracy on the MNIST dataset in hardware-aware artificial neural network simulations. Overall, this work establishes dithiophosphate-derived SnS_2 as a chemically tunable and scalable thin-film platform in which molecular precursor design directly dictates phase formation, film structure, and emergent electronic functionality, offering a viable route toward low-power memristive and neuromorphic systems.

Conflicts of interest

No conflicts of interest exist.

Data availability

Data for this article are available from the University of Southampton repository at https://doi.org/10.5258/SOTON/D3932.

Supplementary information: additional experimental and characterization data, including synthetic procedures for the ligand and SSP, full FT-IR and multinuclear NMR spectra (^1H, $^{31}P\{^1H\}$, and $^{119}Sn\{^1H\}$) of all new compounds, and crystallographic details and refinement parameters for $[Cl_2Sn(S_2P(O^iC_3H_7)_2)_2]$ (Table S1). Additional data include structural and microstructural analysis of SnS_2 thin films, machine learning validation, and comparative device performance (Table S6). See DOI: https://doi.org/10.1039/d6tc00598e.

CCDC 2360486 $[Cl_2Sn(S_2P(O^iC_3H_7)_2)_2]$ contains the supplementary crystallographic data for this paper.[55]

Acknowledgements

The authors would like to thank EPSRC (EP/Y001567/1) for funding this project. The authors also acknowledge Mahindra University (Hyderabad, India) and University of Southampton (Southampton, UK) for the experimental resources utilized in this study. Additionally, appreciation is extended to Sophisticated Analytical Instrument Facilities (SAIF), Punjab University (Chandigarh, India) for granting access to the NMR characterization facility. The SEM facility provided by the School of Physics and SCXRD facility offered by the School of Chemistry, University of Hyderabad, India, are also gratefully acknowledged.

References

1 S. M. Lee, Y. J. Kim, S. J. Park, W. S. Cheon, J. Kim, G. B. Nam, Y. Kim and H. W. Jang, *Adv. Funct. Mater.*, 2025, **35**, 2417019.
2 L. Xu, P. Zhang, H. Jiang, X. Wang, F. Chen, Z. Hu, Y. Gong, L. Shang, J. Zhang, K. Jiang and J. Chu, *Small*, 2019, **15**, 1904116.
3 F. Huang, J. Chen, C. Du, Q. Zhang, Y. Ding and W. Huang, *ACS Appl. Electron. Mater.*, 2022, **4**, 5333–5339.
4 S. Ling, S. Lin, Y. Wu and Y. Li, *Chem. Eng. J.*, 2024, **486**, 150100.
5 T. Sriv, K. Kim and H. Cheong, *Sci. Rep.*, 2018, **8**, 10194.
6 M. J. Loes, A. Lipatov, N. S. Vorobeva, H. Lu, J. Abourahma, D. S. Muratov, A. Gruverman and A. Sinitskii, *ACS Appl. Electron. Mater.*, 2023, **5**, 705–713.
7 H. S. Song, S. L. Li, L. Gao, Y. Xu, K. Ueno, J. Tang, Y. B. Cheng and K. Tsukagoshi, *Nanoscale*, 2013, **5**, 9666–9670.
8 T. G. Hibbert, A. T. Kana, M. F. Mahon, K. C. Molloy, L. S. Price, I. P. Parkin and M. M. Venter, *Main Group Met. Chem.*, 2001, **24**, 633–636.
9 G. Barone, T. G. Hibbert, M. F. Mahon, K. C. Molloy, L. S. Price, I. P. Parkin, A. M. E. Hardy and M. N. Field, *J. Mater. Chem.*, 2001, **11**, 464–468.
10 L. S. Price, I. P. Parkin, M. N. Field, A. M. E. Hardy, R. J. H. Clark, T. G. Hibbert and K. C. Molloy, *J. Mater. Chem.*, 2000, **10**, 527–530.
11 G. Barone, T. Chaplin, T. G. Hibbert, A. T. Kana, M. F. Mahon, K. C. Molloy, I. D. Worsley, I. P. Parkin and L. S. Price, *J. Chem. Soc., Dalton Trans.*, 2002, 1085–1092.
12 A. T. Kana, T. G. Hibbert, M. F. Mahon, K. C. Molloy, I. P. Parkin and L. S. Price, *Polyhedron*, 2001, **20**, 2989–2995.
13 C. M. Song, D. Kim, S. Lee and H. J. Kwon, *Adv. Sci.*, 2024, **11**, 2308588.
14 C. Guo, L. Liu, Z. Cai, Y. Wang, K. Guan, F. Sun, W. Zhou, X. Gou, X. He, X. Wang and T. Zhang, *Microsyst. Nanoeng.*, 2025, **11**, 246.
15 Z. Zhu, G. Hyett, G. Reid, F. Robinson, G. Cibin and A. L. Hector, *Small Struct.*, 2023, **4**, 2200396.
16 Q. Fu, Q. Wu, X. Zhang, Z. Cai, K. K. Ostrikov, X. Gu, H. Nan and S. Xiao, *ACS Appl. Nano Mater.*, 2022, **5**, 14978–14986.
17 Q. A. Vu, H. Kim, V. L. Nguyen, U. Y. Won, S. Adhikari, K. Kim, Y. H. Lee and W. J. Yu, *Adv. Mater.*, 2017, **29**, 1703363.
18 C. Gurnani, S. L. Hawken, A. L. Hector, R. Huang, M. Jura, W. Levason, J. Perkins, G. Reid and G. B. G. Stenning, *Dalton Trans.*, 2018, **47**, 2628–2637.
19 M. A. Malik, N. Revaprasadu and P. O'Brien, *Chem. Mater.*, 2001, **13**, 913–920.
20 A. L. Bingham, J. E. Drake, C. Gurnani, M. B. Hursthouse, M. E. Light, M. Nirwan and R. Ratnani, *J. Chem. Crystallogr.*, 2006, **36**, 627–630.
21 V. Guiot, E. Janod, B. Corraze and L. Cario, *Chem. Mater.*, 2011, **23**, 2611–2618.
22 W. J. Yin, T. Shi and Y. Yan, *Adv. Mater.*, 2014, **26**, 4653–4658.
23 K. J. Kwak, D. E. Lee, S. J. Kim and H. W. Jang, *J. Phys. Chem. Lett.*, 2021, **12**, 8999–9010.
24 Z. Xu, S. Chen, Y. Pan, F. Li, H. Sun, Q. Lu, Y. Li, Y. Bai, Y. Xia, X. Cheng, C. Shi, C. Ma, C. Zhang and Y. Li, *Int. J. Extrem. Manuf.*, 2025, **7**, 025507.
25 Y. Li, Z. Xu, S. Chen, S. Xu, C. Zhang, F. Li, Y. Liu, Q. Lu, X. Cheng, F. Kang, C. L. Ma, Y. Li and Q. Zhang, *Chem. Mater.*, 2025, **37**, 5355–5364.
26 T. R. Desai, R. S. P. Goud, T. D. Dongale and C. Gurnani, *ACS Omega*, 2023, **8**, 48873–48883.
27 Z. Abbas, M. Riaz, S. H. A. Jaffery, S. K. A. Abidi, S. Hussain and J. Jung, *Small*, 2025, **21**, e04294.
28 H. An, Y. Li, Y. Ren, Y. Wan, W. Wang, Z. Sun, J. Zhong and Z. Peng, *Nanoscale*, 2024, **16**, 12142–12148.
29 E. K. Jang, Y. Park and J. S. Lee, *Nanoscale*, 2019, **11**, 15382–15388.
30 Y. Wu, S. Li, Y. Ji, Z. Weng, H. Xing, L. Arauz, T. Hu, J. Hong, K. W. Ang and S. Liu, *Sci. China Mater.*, 2025, **68**, 581–589.
31 J. Feng, J. Fan, Z. Zhang, Y. Gao, S. Xue, G. Cai and J. S. Zhao, *Adv. Funct. Mater.*, 2024, **34**, 2401228.
32 S. S. Harke, T. Zhang, R. Huang and C. Gurnani, *Mater. Adv.*, 2023, **4**, 4119–4128.
33 G. M. Sheldrick, *Acta Crystallogr., Sect. A: Found. Adv.*, 2015, **71**, 3–8.
34 O. V. Dolomanov, L. J. Bourhis, R. J. Gildea, J. A. K. Howard and H. Puschmann, *J. Appl. Crystallogr.*, 2009, **42**, 339–341.
35 J. S. Yadav, R. K. Mehrotra and G. Srivastava, *Polyhedron*, 1987, **6**, 1687–1693.
36 C. Glidewell, *Inorg. Chim. Acta*, 1977, **25**, 159–163.
37 H. C. Clark, V. K. Jain, R. C. Mehrotra, B. P. Singh, G. Srivastava and T. Birchall, *J. Organomet. Chem.*, 1985, **279**, 385–394.
38 K. C. Molloy, M. B. Hossain, D. Van Der Helm, J. J. Zuckerman and I. Haiduc, *Inorg. Chem.*, 2002, **19**, 2041–2045.
39 R. W. Gable, C. L. Raston, G. L. Rowbottom, A. H. White and G. Winter, *J. Chem. Soc., Dalton Trans.*, 1981, 1392–1397.
40 S. W. Cowan, R. W. Gable, B. F. Hoskins and G. Winter, *Inorg. Chim. Acta*, 1983, **77**, L225–L227.
41 L. Zhuo, Y. Wu, L. Wang, Y. Yu, X. Zhang and F. Zhao, *RSC Adv.*, 2012, **2**, 5084–5087.

42 X. An, J. C. Yu and J. Tang, *J. Mater. Chem. A*, 2013, **2**, 1000–1005.
43 M. Li, E. Liu, H. Hu, S. Ouyang, H. Xu and D. Wang, *Int. J. Photoenergy*, 2014, 394146.
44 B. Luo, Y. Fang, B. Wang, J. Zhou, H. Song and L. Zhi, *Energy Environ. Sci.*, 2012, **5**, 5226–5230.
45 C. Wang, K. Tang, Q. Y. Aa and Y. Qian, *Chem. Phys. Lett.*, 2002, **357**, 371–375.
46 C. Li, D. Belkin, Y. Li, P. Yan, M. Hu, N. Ge, H. Jiang, E. Montgomery, P. Lin, Z. Wang, W. Song, J. P. Strachan, M. Barnell, Q. Wu, R. S. Williams, J. J. Yang and Q. Xia, *Nat. Commun.*, 2018, **9**, 1–8.
47 D. Liu, Z. Tang and Z. Zhang, *Sens. Actuators, B*, 2018, **273**, 473–479.
48 J. Maamria, J. Soli, C. Coperaa, P. Bonnet and E. Elaloui, *Chem. Africa*, 2024, **7**, 5339–5354.
49 N. G. Deshpande, A. A. Sagade, Y. G. Gudage, C. D. Lokhande and R. Sharma, *J. Alloys Compd.*, 2007, **436**, 421–426.
50 Z. Cui, F. R. Poblete and Y. Zhu, *ACS Appl. Mater. Interfaces*, 2019, **11**, 17836–17842.
51 M. Zaheer, T. Aziz, J. Lan, Q. Zhu, W. Wang, M. Shen, F. Zhou, L. Lin, X. Feng and Y. Li, *China Semicond. Technol. Int. Conf. (CSTIC 2023)*, China, 2023.
52 J. Jian, P. Dong, Z. Jian, T. Zhao, C. Miao, H. Chang, J. Chen, Y. F. Chen, Y. Bin Chen, H. Feng and B. Sorli, *ACS Nano*, 2022, **16**, 20445–20456.
53 I. T. Wang, C. C. Chang, L. W. Chiu, T. Chou and T. H. Hou, *Nanotechnology*, 2016, **27**, 365204.
54 W. Liu, L. Hu, R. Zhao, Z. Hou and J. Tian, *Adv. Electron. Mater.*, 2026, **7**, 2500037.
55 CCDC 2360486: Experimental Crystal Structure Determination, 2026, DOI: 10.5517/ccdc.csd.cc2k78qt.